remote sensing

MDPI

Article

Global Moho Gravity Inversion from GOCE Data: Updates and Convergence Assessment of the GEMMA Model Algorithm

Lorenzo Rossi [1,*], Biao Lu [1,2], Mirko Reguzzoni [1], Daniele Sampietro [3], Islam Fadel [2] and Mark van der Meijde [2]

[1] Department of Civil and Environmental Engineering, Politecnico di Milano, 20133 Milan, MI, Italy
[2] Department of Earth System Analysis, University of Twente, 7500 AE Enschede, The Netherlands
[3] Geomatics Research & Development s.r.l., 22074 Lomazzo, CO, Italy
* Correspondence: lorenzo1.rossi@polimi.it

Abstract: Since its discovery in 1909, the Moho was routinely studied by seismological methods. However, from the 1950s, a possible alternative was introduced by gravimetric inversion. Thanks to satellite gravity missions launched from the beginning of the 21st century, a global inversion became feasible, e.g., leading to the computation of the GEMMA model in 2012. This model was computed inverting the GOCE second radial derivatives of the anomalous potential by a Wiener filter, which was applied in the spherical harmonic domain, considering a two-layer model with lateral and vertical density variations. Moreover, seismic information was introduced in the inversion to deal with the joint estimation/correction of both density and geometry of the crustal model. This study aims at revising the GEMMA algorithm from the theoretical point of view, introducing a cleaner formalization and studying the used approximations more thoroughly. The updates are on: (1) the management of the approximations due to the forward operator linearization required for the inversion; (2) the regularization of spherical harmonic coefficients in the inversion by proper modelling the Moho signal and the gravity error covariances; (3) the inclusion of additional parameters and their regularization in the Least Squares adjustment to correct the density model by exploiting seismic information. Thanks to these updates, a significant improvement from the computational point of view is achieved too, thus the convergence of the iterative solution and the differences with respect to the previous algorithm can be assessed by closed-loop tests, showing the algorithm performance in retrieving the simulated "true" Moho.

Keywords: moho discontinuity; gravity inversion; Wiener filter; crustal model; GOCE; GEMMA

Citation: Rossi, L.; Lu, B.; Reguzzoni, M.; Sampietro, D.; Fadel, I.; van der Meijde, M. Global Moho Gravity Inversion from GOCE Data: Updates and Convergence Assessment of the GEMMA Model Algorithm. *Remote Sens.* **2022**, *14*, 5646. https://doi.org/10.3390/rs14225646

Academic Editor: Xiaogong Hu

Received: 5 September 2022
Accepted: 2 November 2022
Published: 9 November 2022

1. Introduction

The Mohorovičić discontinuity or Moho, i.e., the discontinuity surface that approximates the boundary between the Earth's crust and mantle, has been traditionally studied by analysing seismic and seismologic data. In particular, since its discovery in 1909 by Mohorovičić [1] a number of seismologist (starting from Gutenberg, Caloi, Rizova, and others in the 1940s and the 1950s) have studied it by exploiting data acquired by local seismic networks [2]. With the advent of the "deep seismic sounding", especially thanks to the hydrocarbon industry, it became possible to recover seismic sections along several profiles and to estimate the first global Moho map in 1982 [3]. In this respect, a noteworthy result was the CRUST5.1 global model [4] based on seismic refraction and, later on, its updated versions, i.e CRUST2.0 [5] and CRUST1.0 [6]. These models describe the crustal structure by giving information on the thickness and density of a number of global layers (e.g., ice, oceans, soft and hard sediments, upper, middle, and lower crust) on a grid with a resolution of 5°, 2°, and 1°, respectively. Moreover, for each cell of the grid, the crustal type (e.g., oceanic, continental plateaus, rifts, orogenetic regions, etc.), and the crust and the upper mantle densities are also given. The models of the CRUST series are based on seismic

refraction data published from 1950 [7], on a detailed compilation of ice and sediment thickness, and on statistical predictions for regions such as most of Africa, South America, Greenland, and oceans, where no or very few seismic measurements are available.

An alternative tool to study the Moho surface is the use of gravity observations. The first attempts to determine its depth from gravity anomalies date back to the fifties thanks to the work of Heiskanen [8]. In the 1960s, Talwani derived rapid formulas to compute the gravitational effect due to bodies of arbitrary shape and applied them to the estimate of crustal structure of the Earth by means of a trial and error approach [9,10]. In the seventies, Oldenburg [11], rearranging the Parker formula to compute the gravitational anomaly of an uneven, non-uniform layer of material [12], derived an iterative procedure based on the Fast Fourier Transform to retrieve the shape of the density anomaly causing the observed anomalous signal. In the nineties, several methods started to be proposed in the literature, for instance Braitenberg et al. [13] suggested an iterative method based on isostatic assumptions and Barzaghi et al. [14] proposed an inversion method based on a Least-Squares Collocation approach. Since 2000, the availability of satellite gravity observations allows for global inversion of the Moho (see for instance [15–20]), e.g., exploiting a linearized expression relating the undulation of an uneven surface over a reference sphere to the coefficients of a spherical harmonic expansion of the anomalous potential [21,22]. Another possible option for a global inversion is the Moritz's generalization of the Vening-Meinesz inverse problem of isostasy [23–25]. In this context, Reguzzoni and Sampietro [26] improved the method proposed by Barzaghi et al. [14] by extending it from the inversion of gravity anomalies to other functionals of the gravitational potential, such as the potential itself and its first and second vertical derivatives, and by applying it in the frequency domain. This approach, globally applied in the spherical harmonic domain, led to the computation of the global GEMMA model [18].

The goal of this paper is to develop a revised version of the inversion algorithm used to compute the GEMMA model [18,19], also introducing a cleaner formalization from the theoretical point of view, and studying the used approximations more thoroughly. The main updates are on: (1) the management of the approximations due to the forward linearization required for the inversion; (2) the regularization of the spherical harmonic coefficients in the inversion, by proper modelling the Moho undulation signal and the gravity error covariances; (3) the inclusion of additional parameters and their regularization in the Least Squares adjustment designed to correct the density model according to the available seismic observations of the Moho surface. The effects of the updates will be shown through closed-loop simulations, also used to test the algorithm convergence that was not assessed in the GEMMA solution computed in 2015 [18].

The revised version of the algorithm is presented in Sections 2–5, describing the inverse operator, the data reduction required to manage vertical variations in the crustal density profiles, and how the seismic information is introduced in the inversion procedure to correct the a priori density profiles. The setup of the closed-loop tests is presented in Section 6. Sections 7 and 8 show the algorithm convergence tests and the impact of the linearized forward equations used for the inversion, respectively. In Section 9 both the revised and the original inversion algorithms are applied to the same closed-loop scenarios, to verify their consistency and to evaluate their performances in view of computing a new global crustal model exploiting updated input than those of the GEMMA solution. Finally, conclusions and future perspective are drawn in Section 10.

2. The Inversion Operator

Global gravity inversion is usually solved in spherical approximation, by means of spherical coordinates, namely latitude φ or co-latitude ϑ, longitude λ, and radial distance r. According to this approximation, the Moho discontinuity can be thought of as an undulation $\delta R(\vartheta, \lambda)$ with respect to a reference sphere with radius $\bar{R}$. This means that

the Moho discontinuity depth $D(\vartheta, \lambda)$ with respect to the mean Earth radius R_E can be written as:

$$D(\vartheta, \lambda) = R_E - [\bar{R} + \delta R(\vartheta, \lambda)] = \bar{D} - \delta R(\vartheta, \lambda) \quad (1)$$

where $\delta R(\vartheta, \lambda)$ is the Moho undulation, $D(\vartheta, \lambda)$ is positive downward, and $\bar{D}$ is the depth of the reference sphere. To introduce the two-layer approximation, it is required to reduce the data for the effect of the main anomalous masses such as sediments and water (with ρ_S and ρ_W mass densities, respectively), and for the contribution of a layered Earth with a reference Moho equal to a sphere of radius $\bar{R}$ (or depth $\bar{D}$, see Figure 1).

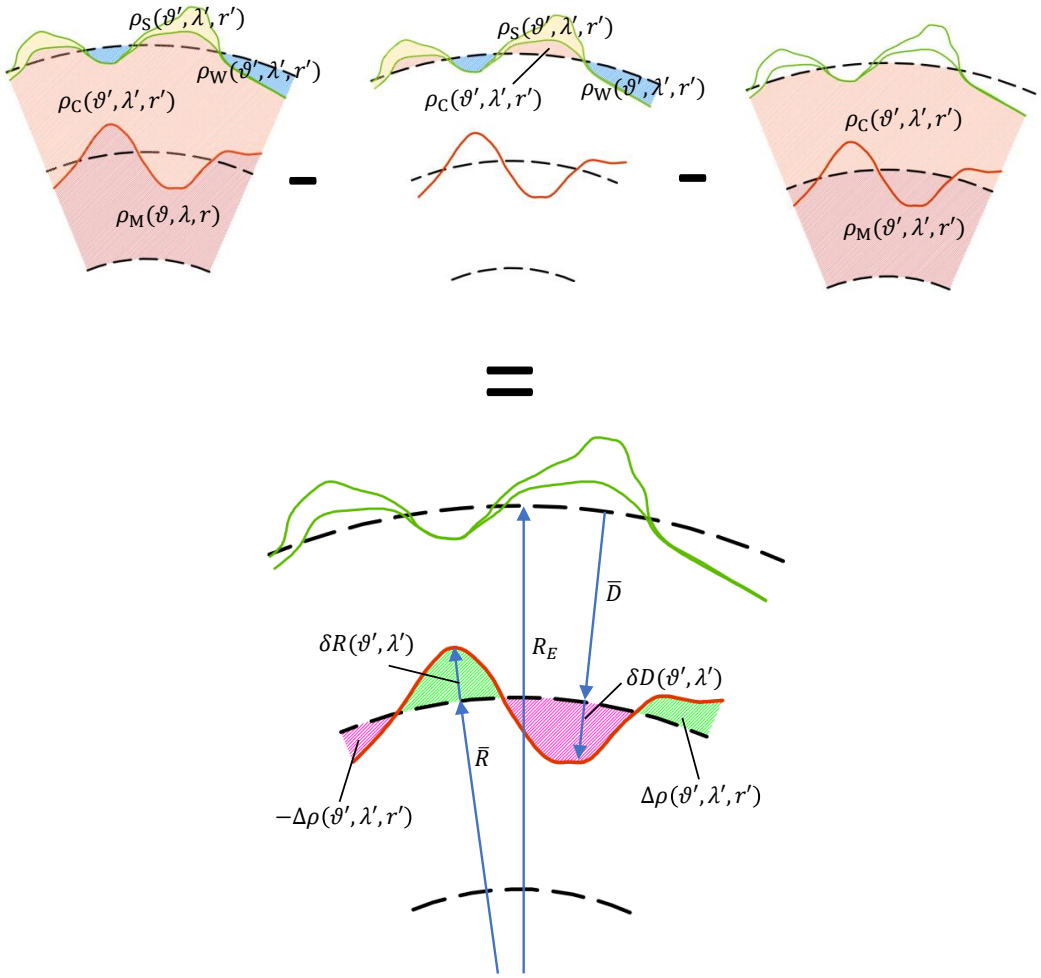

Figure 1. Data reduction to isolate the contribution of the Moho undulation $\delta R(\vartheta', \lambda')$. The geometry of the problem is depicted on the reduced model. The arrows show the positive direction of each quantity.

Considering the obtained spherical two-layer model, the gravitational effect due to the density contrast between crust and mantle inside the Moho undulation at a generic point $P(\vartheta, \lambda, r)$ can be written, in terms of anomalous potential δT, as:

$$\delta T(\vartheta, \lambda, r) = G \iint_{\Sigma} \int_{\bar{R}}^{\bar{R}+\delta R(\vartheta', \lambda')} \frac{\Delta\rho(\vartheta', \lambda', r')}{d(\vartheta, \lambda, r, \vartheta', \lambda', r')} r'^2 dr' d\sigma' \quad (2)$$

where:

- $d(\vartheta, \lambda, r, \vartheta', \lambda', r')$ is the distance between the computational point $P(\vartheta, \lambda, r)$ and the running point inside the masses $Q(\vartheta', \lambda', r')$ that can be expressed as [27]:

$$\frac{1}{d(\vartheta, \lambda, r, \vartheta', \lambda', r')} = \sum_{n=0}^{+\infty} \frac{(r')^n}{r^{n+1}} P_n(\cos\psi) \tag{3}$$

  where $P_n(\cos\psi)$ are the Legendre polynomial of degree n and $\psi = \psi(\vartheta, \lambda, \vartheta', \lambda')$ is the spherical distance between the points P and Q;
- $\Delta\rho(\vartheta', \lambda', r')$ is the density contrast between the crust and mantle at point Q, given the laterally and vertically varying densities of the crust ρ_C and mantle ρ_M, i.e.,:

$$\Delta\rho(\vartheta', \lambda', r') = \rho_M(\vartheta', \lambda', r') - \rho_C(\vartheta', \lambda', r') \; ; \tag{4}$$

- Σ is the integration domain that in our case is a spherical domain;
- $d\sigma' = \sin\vartheta d\lambda d\vartheta$ is the infinitesimal area element over the spherical domain;
- G is the universal gravitational constant.

Now, assuming to deal with a density contrast without any vertical variation, i.e., $\Delta\rho(\vartheta', \lambda', r') = \overline{\Delta\rho}(\vartheta', \lambda') \; \forall \; r'$, we can linearize Equation (2) with respect to δR around the reference Moho $\bar{R}$, i.e., considering $\delta R \approx 0$. By applying the Leibnitz rule to Equation (3), we obtain:

$$\begin{aligned} \delta T(\vartheta, \lambda, r) \approx G \iint_\Sigma \left[\overline{\Delta\rho}(\vartheta', \lambda') \frac{\bar{R}^2}{d(\vartheta, \lambda, r, \vartheta', \lambda', r' = \bar{R})} d\sigma' \right] \delta R(\vartheta', \lambda') = \\ G\bar{R} \iint_\Sigma \overline{\Delta\rho}(\vartheta', \lambda') \delta R(\vartheta', \lambda') \sum_{n=0}^{+\infty} \left(\frac{\bar{R}}{r} \right)^{n+1} P_n(\cos\psi) d\sigma'. \end{aligned} \tag{5}$$

For the sake of simplicity we can define a new variable $\delta\omega(\vartheta', \lambda')$ as the product of the Moho undulation by the density contrast [22]:

$$\delta\omega(\vartheta', \lambda') = \overline{\Delta\rho}(\vartheta', \lambda') \delta R(\vartheta', \lambda') \; . \tag{6}$$

Recalling the summation rule (Equation (7)) and the spherical harmonic analysis operator (Equation (8)):

$$P_n(\cos\psi) = \frac{\sum_m Y_{nm}(\vartheta, \lambda) Y_{nm}(\vartheta', \lambda')}{2n+1} \; , \tag{7}$$

$$\delta\omega_{nm} = \frac{1}{4\pi} \int \int_\Sigma \delta\omega(\varphi', \lambda') Y_{nm}(\vartheta', \lambda') d\sigma' \; , \tag{8}$$

where n is degree, m is the order and $Y_{nm}(\vartheta, \lambda)$ are the spherical harmonic functions, we can introduce Equation (6) into Equation (5), obtaining:

$$\delta T(\vartheta, \lambda, r) = 4\pi G\bar{R} \sum_n \left(\frac{\bar{R}}{r} \right)^{n+1} \frac{1}{2n+1} \sum_m \delta\omega_{nm} Y_{nm}(\vartheta, \lambda) \; . \tag{9}$$

We can now derive the relation between the spherical harmonic coefficients of the gravitational potential δT and the ones of $\delta\omega$, by firstly recalling the classical spherical harmonic expansion of the gravitational potential [27]:

$$\delta T(\vartheta, \lambda, r) = \frac{GM_E}{R_E} \sum_n \left(\frac{R_E}{r} \right)^{n+1} \sum_m \delta T_{nm} Y_{nm}(\vartheta, \lambda) \tag{10}$$

where M_E is the total mass of the Earth. Then, by imposing the equality condition between Equations (9) and (10), we obtain [19,22]:

$$\delta T_{nm} = \frac{3}{\rho_E \bar{R}} \left(\frac{\bar{R}}{R_E} \right)^{n+3} \frac{\delta\omega_{nm}}{2n+1} = \frac{1}{\rho_E \bar{R}} \frac{\delta\omega_{nm}}{\beta_n} = K_n \delta\omega_{nm} \; , \tag{11}$$

where ρ_E is the mean density of the Earth depending on M_E and R_E and, accordingly to the GEMMA algorithm [19]:

$$\beta_n = \frac{2n+1}{3(1-\bar{D}/R_E)^{n+3}} \,. \tag{12}$$

Consequently, we obtain:

$$K_n = \frac{1}{\rho_E \bar{R} \beta_n} = \frac{3}{\rho_E \bar{R}(2n+1)} \left(\frac{\bar{R}}{R_E}\right)^{n+3} \,. \tag{13}$$

Starting from the linearized forward operator of Equation (11), we can derive an inversion operator $\mathcal{I}(\cdot)$ to estimate the spherical harmonic coefficients of the product between the Moho undulation and the density contrast from the coefficients of the observed gravitational potential, i.e.,:

$$\widehat{\delta\omega}_{nm} = \mathcal{I}\left(\delta T^{\text{obs}}_{nm}\right) \,. \tag{14}$$

Here, we assume that the observed functional of the gravity signal, e.g., the second radial derivative $\delta T^{\text{obs}}_{rr}(\vartheta,\lambda)$, has been already reduced to isolate the signal of the Moho undulation only (consistently with the forward modelling presented in Equation (2)) and analysed to reckon the gravitational potential spherical harmonic coefficients $\delta T^{\text{obs}}_{nm}$. We leave further details about the reduction of the real gravity observations to Section 3.

Then, assuming to know the density contrast and recalling Equation (6), we can estimate the Moho surface as:

$$\widehat{D}(\vartheta,\lambda) = R_E - \left[\bar{R} + \frac{\widehat{\delta\omega}(\vartheta,\lambda)}{\overline{\Delta\rho}(\vartheta,\lambda)}\right] = \bar{D} - \frac{\widehat{\delta\omega}(\vartheta,\lambda)}{\overline{\Delta\rho}(\vartheta,\lambda)} = \bar{D} - \frac{\sum_n \sum_m \widehat{\delta\omega}_{nm} Y_{nm}(\vartheta,\lambda)}{\overline{\Delta\rho}(\vartheta,\lambda)} \,. \tag{15}$$

Since Equation (11) is a linear expression in its general form, the operator $\mathcal{I}\left(\delta T^{\text{obs}}_{nm}\right)$ presented in Equation (14) could be straightforwardly derived as:

$$\widehat{\delta\omega}_{nm} = \rho_E \bar{R} \beta_n \delta T_{nm} = \frac{1}{K_n} \delta T^{\text{obs}}_{nm} \,. \tag{16}$$

However, this inverse operator is strongly unstable and can significantly amplify the noise of the observed gravitational signal [19]. To overcome this problem, a regularization is required. According to the Wiener–Kolmogorov principle, i.e., the minimization of the mean square estimation error, the optimal regularization can be found by implementing a Wiener filter [28] and therefore using the following inversion operator:

$$\widehat{\delta\omega}_{nm} = \frac{K_n \sigma^2_{\delta\omega_n}}{K_n^2 \sigma^2_{\delta\omega,n} + \sigma^2_{\nu,n}} \delta T^{\text{obs}}_{nm} \,, \tag{17}$$

where, under the assumption to deal with homogeneous and isotropic fields, $\sigma^2_{\delta\omega,n}$ and $\sigma^2_{\nu,n}$ are the degree variances of $\delta\omega$ and the observation noise ν, respectively.

It is worth to remark that Equation (17) is a generalization with respect to the solution of the original GEMMA algorithm, in which the estimation of the spherical harmonic coefficients $\widehat{\delta\omega}_{nm}$ was performed in two steps: the first one was the straightforward transformation of the spherical harmonic coefficients of the observed gravity potential $\delta T^{\text{obs}}_{nm}$ by means of Equation (16), the second one was a regularization of $\widehat{\delta\omega}_{nm}$ by means of a Wiener filter. The implemented generalization simplifies the way in which the input to the Wiener filter has to be supplied. In fact, it is enough to know the covariance function of $\delta\omega$, e.g., by exploiting geological a priori information, and of the observation noise, usually directly provided with the global gravity model coefficients to be inverted. The previous approach, instead, required to propagate the covariance function of the observed gravity signal to

$\delta\omega$ (e.g., by means of Monte Carlo samples) in order to setup a proper regularization. Furthermore, it has to be stressed that Equation (17) represents the solution of the Wiener filter assuming that the noise of the signal can be expressed in terms of degree variances. This is not generally true and a more reliable filter can be implemented by considering e.g., the variances of the spherical harmonic coefficients that are usually provided with global models, or even the (block diagonal) error covariance matrix of the coefficients.

3. The Data Reduction

We assume to work with satellite-based observations, i.e., the ones coming from the GOCE mission [29,30], after the reduction for the contribution of the normal gravity field. This can be interpreted as the subtraction of the contribution of the global Earth mass assuming that it is homogeneously distributed over layers with ellipsoidal boundaries and allows to treat the problem in spherical approximation. To isolate the effect of the Moho undulation we have to remove the effect of the known mass anomalies above the crystalline basement from the anomalous observations. Considering the second radial derivative of the gravitational potential, we obtain:

$$T_{rr}^{\text{res}}(\vartheta,\lambda) = T_{rr}^{\text{obs}}(\vartheta,\lambda) - T_{rr}^{\text{ice}}(\vartheta,\lambda) - T_{rr}^{\text{oce}}(\vartheta,\lambda) - T_{rr}^{\text{sed}}(\vartheta,\lambda) \tag{18}$$

where $T_{rr}^{\text{obs}}(\vartheta,\lambda)$ is the observation at satellite altitude, T_{rr}^{ice}, T_{rr}^{oce}, and T_{rr}^{sed} the effect of oceanic masses, ice sheets and sediments, respectively, assuming to know their density and shape. The dependency from r is omitted, since we assumed to work with gridded data at a constant radial distance $r = R_E + h_{\text{sat}}$, where h_{sat} is the mean satellite altitude.

The effect of the anomalous masses of the layer ℓ (in Equation (18) ℓ = ice, oce, sed), in terms of second radial derivative of the gravitational potential, can be computed as:

$$T_{rr}^{\ell}(\vartheta,\lambda) = \mathcal{F}_{rr}\Big(\rho_{\ell}(\vartheta',\lambda',r'), r_{\ell}^{\text{T}}(\vartheta',\lambda'), r_{\ell}^{\text{B}}(\vartheta',\lambda'), \vartheta, \lambda\Big) \tag{19}$$

where $\mathcal{F}_{rr}(\cdot)$ is the forward operator, e.g., based on point masses numerical integration, depending on the density distribution of the layer $\rho_{\ell}(\vartheta',\lambda',r')$ and its top and bottom boundary surfaces $r_{\ell}^{\text{T}}(\vartheta',\lambda')$ and $r_{\ell}^{\text{B}}(\vartheta',\lambda')$, respectively. Note that, by directly using the actual density $\rho_{\ell}(\vartheta',\lambda',r')$ instead of the density contrast, the resulting forward modelling changes by a constant value thanks to the spherical approximation. This constant effect will be managed during the inversion procedure (see Section 4).

In order to apply Equation (17), the contribution of the Moho undulation only has to be isolated. To this aim, a further reduction of the observations is required to remove the contribution of crystalline crust and upper mantle, above and below the linearization radius $\bar{R}$, respectively. Nevertheless, consistently to Equation (17), this reduction can be performed only if there are no vertical variations in crust and mantle densities, i.e., considering two densities $\overline{\rho}_{\text{C}}(\vartheta',\lambda')$ and $\overline{\rho}_{\text{M}}(\vartheta',\lambda')$, respectively. This assumption lead to the following reduction:

$$\begin{aligned}\delta T_{rr}^{\text{obs}}(\vartheta,\lambda) = T_{rr}^{\text{res}}(\vartheta,\lambda) &- \mathcal{F}_{rr}(\overline{\rho}_{\text{C}}(\vartheta',\lambda'), r_{\text{C}}^{\text{T}}(\vartheta',\lambda'), \bar{R}, \vartheta, \lambda) \\ &- \mathcal{F}_{rr}(\overline{\rho}_{\text{M}}(\vartheta',\lambda'), \bar{R}, r_{\text{M}}^{\text{B}}, \vartheta, \lambda)\ .\end{aligned} \tag{20}$$

Note that also in this case the reduction is performed apart from a constant, recalling that we are working in spherical approximation, and that no further density anomalies are considered below the bottom of the upper mantle r_{M}^{B}. The reduced gridded observations coming from Equation (20) can be analysed to retrieve the spherical harmonic coefficients of the potential $\delta T_{nm}^{\text{obs}}$ to be used in Equation (17).

However, considering lateral variations only is usually too approximated. On the other hand, this condition is strictly required by the linearization introduced into Equation (5), thus not allowing to apply the inversion algorithm in presence of vertical density variations. A possible solution is to apply a further reduction step, "replacing" the vertical varying densities $\rho_{\text{C}}(\vartheta,\lambda,r)$ and $\rho_{\text{M}}(\vartheta,\lambda,r)$ inside the Moho undulation with some approximated

lateral only varying densities $\overline{\rho}_{\mathrm{C}}(\vartheta,\lambda)$ and $\overline{\rho}_{\mathrm{M}}(\vartheta,\lambda)$. This leads to the following expression of the observed signal:

$$\begin{aligned}
&\delta T_{rr}^{\mathrm{obs}}(\vartheta,\lambda) = T_{rr}^{\mathrm{res}}(\vartheta,\lambda) - \mathcal{F}_{rr}\big(\rho_{\mathrm{C}}(\vartheta',\lambda',r'), r_{\mathrm{C}}^{\mathrm{T}}(\vartheta',\lambda'), \bar{R}, \vartheta, \lambda\big)\\
&-\mathcal{F}_{rr}\big(\rho_{\mathrm{M}}(\vartheta',\lambda',r'), \bar{R}, r_{\mathrm{M}}^{\mathrm{B}}, \vartheta, \lambda\big) + \mathcal{F}_{rr}\Big(\rho_{\mathrm{C}}(\vartheta',\lambda',r'), \bar{R}+\widetilde{\delta R}(\vartheta',\lambda'), \bar{R}, \vartheta, \lambda\Big)\\
&+\mathcal{F}_{rr}\Big(\rho_{\mathrm{M}}(\vartheta',\lambda',r'), \bar{R}, \bar{R}+\widetilde{\delta R}(\vartheta',\lambda'), \vartheta, \lambda\Big) - \widetilde{\mathcal{F}}_{rr}\Big(\overline{\rho}_{\mathrm{C}}(\vartheta',\lambda'), \bar{R}+\widetilde{\delta R}(\vartheta',\lambda'), \bar{R}, \vartheta, \lambda\Big)\\
&-\widetilde{\mathcal{F}}_{rr}\Big(\overline{\rho}_{\mathrm{M}}(\vartheta',\lambda'), \bar{R}, \bar{R}+\widetilde{\delta R}(\vartheta',\lambda'), \vartheta, \lambda\Big)\\
&= T_{rr}^{\mathrm{res}}(\vartheta,\lambda) - \mathcal{F}_{rr}\Big(\rho_{\mathrm{C}}(\vartheta',\lambda',r'), r_{\mathrm{C}}^{\mathrm{T}}(\vartheta',\lambda'), \bar{R}+\widetilde{\delta R}(\vartheta',\lambda'), \vartheta, \lambda\Big)\\
&-\mathcal{F}_{rr}\Big(\rho_{\mathrm{M}}(\vartheta',\lambda',r'), \bar{R}+\widetilde{\delta R}(\vartheta',\lambda'), r_{\mathrm{M}}^{\mathrm{B}}, \vartheta, \lambda\Big)\\
&+\widetilde{\mathcal{F}}_{rr}\Big(\overline{\rho}_{\mathrm{C}}(\vartheta',\lambda'), \bar{R}, \bar{R}+\widetilde{\delta R}(\vartheta',\lambda'), \vartheta, \lambda\Big) + \widetilde{\mathcal{F}}_{rr}\Big(\overline{\rho}_{\mathrm{M}}(\vartheta',\lambda'), \bar{R}+\widetilde{\delta R}(\vartheta',\lambda'), \bar{R}, \vartheta, \lambda\Big)
\end{aligned} \tag{21}$$

where $\widetilde{\delta R}(\vartheta',\lambda')$ is an approximated Moho undulation, $\mathcal{F}_{rr}(\cdot)$ is the previously mentioned forward operator (see Equation (19)), $\widetilde{\mathcal{F}}_{rr}(\cdot)$ the linearized forward operator, defined by deriving Equation (9) two times with respect to the radial direction, and where forwards with the same operator and the same density model are grouped by changing the boundaries of the integral, leading to the scheme of Figure 2. By following this strategy, the inversion operator can be applied even in presence of vertical density variations, also taking into account the approximation introduced by the linearized forward operator. It is worth to notice that Equation (21) depends on an approximated value of the Moho undulation $\widetilde{\delta R}(\vartheta',\lambda')$, therefore an iterative procedure is needed to estimate the undulation, assuming the previous iteration Moho undulation estimate as $\widetilde{\delta R}(\vartheta',\lambda')$.

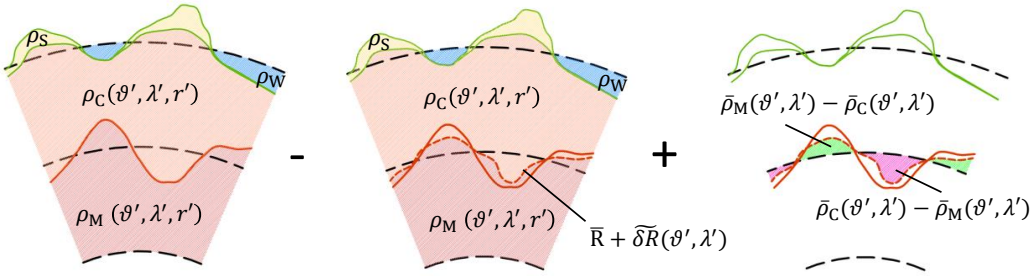

Figure 2. Scheme of the updated data reduction procedure according to Equation (21), considering also vertical density variations. The approximated shape of the Moho undulation $\widetilde{\delta R}(\vartheta',\lambda')$, required for the iterative procedure, is depicted with a red dashed line.

As for the value of the laterally only varying densities $\overline{\rho}_{\mathrm{C}}(\vartheta,\lambda)$ and $\overline{\rho}_{\mathrm{M}}(\vartheta,\lambda)$, a possibility is to compute them as the mean value inside the Moho undulation, namely:

$$\begin{cases}
\overline{\rho}_{\mathrm{C}}(\vartheta,\lambda) = \dfrac{1}{\delta R(\vartheta,\lambda)} \displaystyle\int_{\bar{R}}^{\bar{R}+\delta R(\vartheta,\lambda)} \rho_{\mathrm{C}}(\vartheta,\lambda,r)\mathrm{d}r\\
\overline{\rho}_{\mathrm{M}}(\vartheta,\lambda) = \dfrac{1}{\delta R(\vartheta,\lambda)} \displaystyle\int_{\bar{R}}^{\bar{R}+\delta R(\vartheta,\lambda)} \rho_{\mathrm{M}}(\vartheta,\lambda,r)\mathrm{d}r\,.
\end{cases} \tag{22}$$

Note that these densities depend on $\delta R(\vartheta,\lambda)$, therefore they have to be updated at each iteration too.

4. Seismic Data Integration

In principle, when we reduced the observed signal by means of Equations (18) and (21) we are working with anomalous quantity. However, we removed the effect of the anomalous masses (ice shields, oceans, sediments, crystalline crust, and upper mantle) by introducing their actual density values, without making any hypothesis on the mass distribution of the Earth generating the normal potential. Given the total Earth mass and choosing the

reference ellipsoid (e.g., WGS84), there exists one and only one normal potential [27], but infinite mass distributions inside the ellipsoid generating the same normal potential. It has to be stressed that considering anomalous quantities allows to work in spherical approximation. Therefore, changing the reference (layered) Earth mass density by a constant would result in changing $\delta T_{rr}^{\text{obs}}$ by a constant too. According to the inversion operator (Equation (17)), this would result in changing the $\widehat{\delta\omega}$ estimate by a constant value.

To face this problem we can proceed in two ways: the former is to assume an Earth mass distribution generating the normal potential, e.g., by introducing the PREM model [31], the latter is to estimate the constant to be added to $\delta\omega$ by means of external data sources, e.g., seismic observations of the Moho surface. The first strategy makes the solution dependent from the chosen density model, while the latter allows to rely on an independent set of observations, which is generally preferable. Therefore, the constant μ_ω is introduced in Equation (15) to solve this problem, obtaining:

$$\widehat{D}(\vartheta,\lambda) = \bar{D} - \frac{\widehat{\delta\omega}(\vartheta,\lambda) + \mu_\omega}{\overline{\Delta\rho}(\vartheta,\lambda)}\,. \tag{23}$$

If at least one seismic observation of the Moho surface depth $D^{\text{obs}}(\vartheta,\lambda)$ is available, it can be used into Equation (23) to estimate

$$\hat{\mu}_\omega = \left(D^{\text{obs}}(\vartheta,\lambda) - \bar{D}\right)\overline{\Delta\rho}(\vartheta,\lambda) + \widehat{\delta\omega}(\vartheta,\lambda) \tag{24}$$

where $\overline{\Delta\rho}(\vartheta,\lambda) = \bar{\rho}_{\text{M}}(\vartheta,\lambda) - \bar{\rho}_{\text{C}}(\vartheta,\lambda)$ and $\widehat{\delta\omega}(\vartheta,\lambda)$ is synthesized from the spherical harmonic coefficients estimated by Equation (17). If more than one seismic observation is available, a set of Equation (24) can be used to estimate $\hat{\mu}_\omega$ by means of the Least Squares principle. When the iterative procedure required by Equation (18) to properly manage vertical density variation is started, the estimation of μ_ω has to be repeated at each iteration to update the estimate of $\delta R(\vartheta',\lambda')$.

Moreover, we have to consider the non-perfect knowledge of the density models used for the inversion. To make them more flexible and exploiting a priori information on Moho depth, the crystalline crust above the Moho surface can be divided into a set of "geological provinces", i.e., regions where all points have the same density profile along the vertical direction. Examples of such geological provinces and the corresponding functions relating the mass density with the depth can be found in Mooney et al. [32]. Since these functions are just approximated, they could be "calibrated" by introducing two parameters for each province i, namely a scale factor h_i and a bias k_i. According to these hypotheses, the crustal density can be modelled as follows:

$$\rho_{\text{C}}(\vartheta,\lambda,r) = \sum_{i=1}^{N}(h_i\rho_{\text{C},i}(r) + k_i)\chi_i(\vartheta,\lambda) \tag{25}$$

where $i = 1,2,\ldots,N$ is the index identifying the geological province, $\chi_i(\vartheta,\lambda)$ is the characteristic function defining the domain of the geological province, $\rho_{\text{C},i}(r)$ is the given density profile and (h_i,k_i) are the corresponding scale factor and bias. Note that the choice of applying a linear transformation to the a priori density profiles is not driven by any geophysical motivation, but to the need of leaving the "shape" of the profiles unmodified. Moreover, recalling the linearity of the forward operator with respect to the densities, we can generalize the data reduction in Equation (21) as:

$$\begin{aligned}
&\delta T_{rr}^{\mathrm{obs}}(\vartheta,\lambda) = T_{rr}^{\mathrm{res}}(\vartheta,\lambda) - \mathcal{F}_{rr}\big(\rho_{\mathrm{M}}(\vartheta',\lambda',r'),\bar{R}+\delta R(\vartheta',\lambda'),r_{\mathrm{M}}^{\mathrm{B}},\vartheta,\lambda\big)\\
&-\textstyle\sum_{i=1}^{N}\big[h_i\mathcal{F}_{rr}\big(\rho_{\mathrm{C}}(r')\chi_i(\vartheta',\lambda'),r_{\mathrm{C}}^{\mathrm{T}}(\vartheta',\lambda'),\bar{R}+\delta R(\vartheta',\lambda'),\vartheta,\lambda\big)\\
&+k_i\mathcal{F}_{rr}\big(\chi_i(\vartheta',\lambda'),r_{\mathrm{C}}^{\mathrm{T}}(\vartheta',\lambda'),\bar{R}+\delta R(\vartheta',\lambda'),\vartheta,\lambda\big)\big]\\
&-\textstyle\sum_{i=1}^{N}\Big[h_i\widetilde{\mathcal{F}}_{rr}\Big(\overline{\rho}_{\mathrm{C},i}(\vartheta',\lambda')\chi_i(\vartheta',\lambda'),\bar{R}+\delta R(\vartheta',\lambda'),\bar{R},\vartheta,\lambda\Big)\\
&+k_i\widetilde{\mathcal{F}}_{rr}\big(\chi_i(\vartheta',\lambda'),\bar{R}+\delta R(\vartheta',\lambda'),\bar{R},\vartheta,\lambda\big)\Big]\\
&-\widetilde{\mathcal{F}}_{rr}\big(\overline{\rho}_{\mathrm{M}}(\vartheta',\lambda'),\bar{R},\bar{R}+\delta R(\vartheta',\lambda'),\vartheta,\lambda\big),
\end{aligned} \tag{26}$$

where $\overline{\rho}_{\mathrm{C,i}}(\vartheta',\lambda')$ is computed by applying Equation (22) to the crustal density obtained introducing the density profiles $\rho_{\mathrm{C,i}}(r')$ into Equation (25) fixing $h_i = 1, k_i = 0\ \forall\ i$. Calling $\mathcal{A}_{rr}(\cdot)$ the spherical harmonic analysis operator to derive the potential coefficients from its second radial derivative [27], namely:

$$\mathcal{A}_{rr}(T_{rr}(\vartheta,\lambda)) = \frac{r^{n+3}}{GM_E R_E^{n+3}(n+1)(n+2)}\iint_{\Sigma} T_{rr}(\vartheta,\lambda)Y_{nm}(\vartheta,\lambda)\mathrm{d}\sigma \tag{27}$$

for the sake of notation simplicity, we can define the following quantities:

$$\begin{cases}
T_{nm}^{\mathrm{res}} = \mathcal{A}_{rr}(T_{rr}^{\mathrm{res}}(\vartheta,\lambda))\\
T_{nm}^{\mathrm{C},i} = \mathcal{A}_{rr}\big(\mathcal{F}_{rr}\big(\rho_{\mathrm{C}}(r')\chi_i(\vartheta',\lambda'),r_{\mathrm{C}}^{\mathrm{T}}(\vartheta',\lambda'),\bar{R}+\delta R(\vartheta',\lambda'),\vartheta,\lambda\big)\big)\\
T_{nm}^{1,i} = \mathcal{A}_{rr}\big(\mathcal{F}_{rr}\big(\chi_i(\vartheta',\lambda'),r_{\mathrm{C}}^{\mathrm{T}}(\vartheta',\lambda'),\bar{R}+\delta R(\vartheta',\lambda'),\vartheta,\lambda\big)\big)\\
T_{nm}^{\mathrm{M}} = \mathcal{A}_{rr}\big(\mathcal{F}_{rr}\big(\rho_{\mathrm{M}}(\vartheta',\lambda',r'),\bar{R}+\delta R(\vartheta',\lambda'),r_{\mathrm{M}}^{\mathrm{B}}(\vartheta',\lambda')\vartheta,\lambda\big)\big)\\
\widetilde{T}_{nm}^{\mathrm{C},i} = \mathcal{A}_{rr}\Big(\widetilde{\mathcal{F}}_{rr}\Big(\overline{\rho}_{\mathrm{C},i}\chi_i(\vartheta',\lambda'),\bar{R}+\delta R(\vartheta',\lambda'),\bar{R},\vartheta,\lambda\Big)\Big)\\
\widetilde{T}_{nm}^{1,i} = \mathcal{A}_{rr}\Big(\widetilde{\mathcal{F}}_{rr}\big(\chi_i(\vartheta',\lambda'),\bar{R}+\delta R(\vartheta',\lambda'),\bar{R},\vartheta,\lambda\big)\Big)\\
\widetilde{T}_{nm}^{\mathrm{M}} = \mathcal{A}_{rr}\Big(\widetilde{\mathcal{F}}_{rr}\big(\overline{\rho}_{\mathrm{M}}(\vartheta',\lambda'),\bar{R},\bar{R}+\delta R(\vartheta',\lambda'),\vartheta,\lambda\big)\Big)
\end{cases} \tag{28}$$

Now, recalling that the inversion operator $\mathcal{I}(\cdot)$ is linear, we obtain:

$$\begin{aligned}
&\widehat{\delta}\omega_{nm} = \mathcal{I}(T_{nm}^{\mathrm{res}}) - \mathcal{I}(T_{nm}^{\mathrm{M}}) - \textstyle\sum_{i=1}^{N}\Big[h_i\mathcal{I}\Big(T_{nm}^{\mathrm{C},i}\Big) + k_i\mathcal{I}\Big(T_{nm}^{1,i}\Big)\Big]\\
&-\textstyle\sum_{i=1}^{N}\Big[h_i\mathcal{I}\Big(\widetilde{T}_{nm}^{\mathrm{C},i}\Big) + k_i\mathcal{I}\Big(\widetilde{T}_{nm}^{1,i}\Big)\Big] - \mathcal{I}\Big(\widetilde{T}_{nm}^{\mathrm{M}}\Big)\\
&= \widehat{\omega}^{\mathrm{res}}(\vartheta,\lambda) - \widehat{\omega}^{\mathrm{M}}(\vartheta,\lambda) - \textstyle\sum_{i=1}^{N}\big[h_i\widehat{\omega}^{\mathrm{C,i}}(\vartheta,\lambda) + k_i\widehat{\omega}^{1,\mathrm{i}}(\vartheta,\lambda)\big]\\
&-\textstyle\sum_{i=1}^{N}\Big[h_i\widehat{\widetilde{\omega}}^{\mathrm{C,i}}(\vartheta,\lambda) + k_i\widehat{\widetilde{\omega}}^{1,\mathrm{i}}(\vartheta,\lambda)\Big] - \widehat{\widetilde{\omega}}^{\mathrm{M}}(\vartheta,\lambda)
\end{aligned} \tag{29}$$

where $\widehat{\omega}^{\ell}(\vartheta,\lambda)$ and $\widehat{\widetilde{\omega}}^{\ell}(\vartheta,\lambda)$ represent the synthesis of the coefficients computed applying the corresponding inversion operator $\mathcal{I}\Big(T_{nm}^{\ell}\Big)$ or $\mathcal{I}\Big(\widetilde{T}_{nm}^{\ell}\Big)$ on the computational points, i.e.,:

$$\begin{cases}
\widehat{\omega}^{\ell}(\vartheta,\lambda) = \sum_n\sum_m \mathcal{I}\Big(T_{nm}^{\ell}\Big)Y_{nm}(\vartheta,\lambda)\\
\widehat{\widetilde{\omega}}^{\ell}(\vartheta,\lambda) = \sum_n\sum_m \mathcal{I}\Big(\widetilde{T}_{nm}^{\ell}\Big)Y_{nm}(\vartheta,\lambda)
\end{cases} \tag{30}$$

Moreover, the spherical harmonic analysis operator is linear. Therefore, we can replace $\widehat{\delta\omega}$ in Equation (23) with the synthesis of the terms of Equation (29) and compute the Moho depth as:

$$\widehat{D}(\vartheta,\lambda) = \bar{D} - \frac{\widehat{\omega}^{\mathrm{res}}(\vartheta,\lambda) - \widehat{\omega}^{\mathrm{M}}(\vartheta,\lambda) - \sum_{i=1}^{N}\left[h_i\widehat{\omega}^{\mathrm{C,i}}(\vartheta,\lambda) + k_i\widehat{\omega}^{\mathrm{1,i}}(\vartheta,\lambda)\right]}{\bar{\rho}_{\mathrm{M}}(\vartheta,\lambda) - \sum_{i=1}^{N}\left(h_i\bar{\rho}_{\mathrm{C,i}}(\vartheta,\lambda) + k_i\right)\chi_i(\vartheta,\lambda)} - \frac{-\sum_{i=1}^{N}\left[h_i\widehat{\widetilde{\omega}}^{\mathrm{C,i}}(\vartheta,\lambda) + k_i\widehat{\widetilde{\omega}}^{\mathrm{1,i}}(\vartheta,\lambda)\right] - \widehat{\widetilde{\omega}}^{\mathrm{M}}(\vartheta,\lambda) + \mu_\omega}{\bar{\rho}_{\mathrm{M}}(\vartheta,\lambda) - \sum_{i=1}^{N}\left(h_i\bar{\rho}_{\mathrm{C,i}}(\vartheta,\lambda) + k_i\right)\chi_i(\vartheta,\lambda)}. \quad (31)$$

If seismic observations of the Moho surface are available, starting from Equation (31) a joint estimate of the scale factors h_i, the biases k_i and the constant μ_ω applying the Least Squares principle can be performed, thus generalizing the solution presented in Equation (24) for the estimation of the μ_ω parameter only. Note that this Least Squares system requires a regularization to prevent unphysical estimates of biases and scale factors. To this aim, for each geological province we introduced pseudo-observations of the expected values of crustal density at ground, of crust-mantle density contrast at the Moho, and of the h_k scale factors (that should be close to 1). These pseudo-observations are weighted according to the a priori level of geophysical knowledge.

It is worth to recall that, as it happens in Equation (21), the laterally only varying densities depend on the Moho undulation $\delta R(\vartheta,\lambda)$, i.e., $\bar{\rho}_{\mathrm{C,i}}(\vartheta,\lambda)$, $\bar{\rho}_{\mathrm{M}}(\vartheta,\lambda)$, $\widehat{\omega}^{\mathrm{C},i}(\vartheta,\lambda)$, $\widehat{\omega}^{\mathrm{1},i}(\vartheta,\lambda)$, $\widehat{\omega}^{\mathrm{M}}(\vartheta,\lambda)$, $\widehat{\widetilde{\omega}}^{\mathrm{C,i}}$, $\widehat{\widetilde{\omega}}^{\mathrm{1,i}}$ and $\widehat{\widetilde{\omega}}^{\mathrm{C,i}}$ depend on $\delta R(\vartheta,\lambda)$ (see Equations (28) and (29)). This dependency implies a non-linearity in the system, thus requiring an iterative solution starting, e.g., from $\delta R(\vartheta,\lambda) = 0 \ \ \forall(\vartheta,\lambda)$ or from an a priori model.

5. Overall Scheme of the Inversion Algorithm

Combining all the steps presented into Sections 2–4 we can define the revised inversion algorithm according to the flow chart depicted in Figure 3 to summarize the whole procedure.

The main differences of the presented algorithm with respect to the "original" one, used to compute the GEMMA model in 2015 [18], are related to the data reduction described in Equation (21) and to the density modelling introduced in Equation (25). In particular, the way in which the data reduction is performed allows to consider also the approximation related to the linearized forward $\widetilde{\mathcal{F}}(\cdot)$. This was not performed with the older formulation of the algorithm, where a further reference Moho refinement step was applied after the inversion by inverting the gravity residuals (see Section 2.4 of [18]). This step increases the computational burden of the algorithm and is not completely rigorous with the formalization of the procedure. The non-strictly need of this further step in the presented algorithm will be shown by a numerical example in Section 8.

The scheme highlights how to use the equations in the inversion procedure, which data reduction steps can be performed once and for all before the inversion procedure and which must be performed iteratively, due to their dependency on the current estimation of the Moho surface depth.

As for the vertical density profiles, only scale factors were considered for their adjustment in the original algorithm. Therefore, the new formulation is more general introducing both a scale factor and a bias for each geological province.

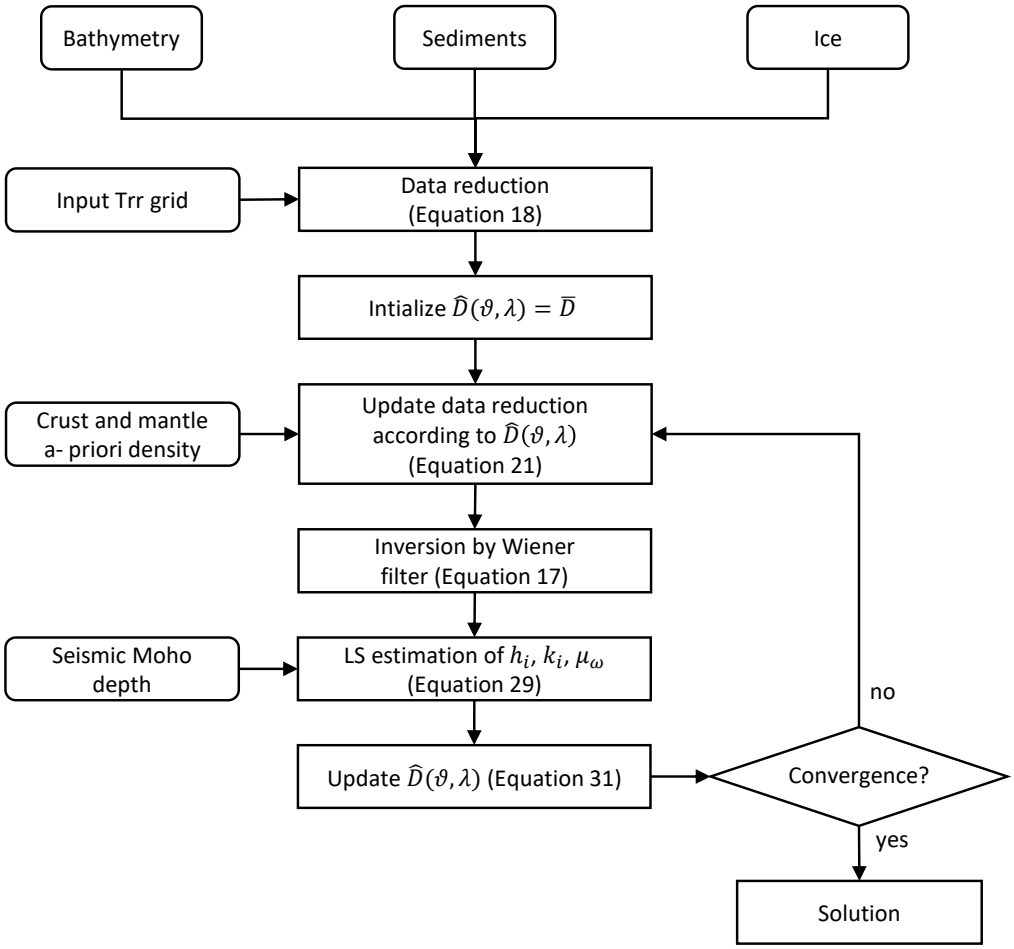

Figure 3. Flow chart of the algorithm.

6. Closed-Loop Test Setup

The performances and the convergence of the iterative inversion algorithm were tested by means of closed-loop tests. Starting from a known model of the Earth, we generated the corresponding gravitational signal in terms of second radial derivative of the anomalous potential and then we inverted it. The inversion was performed by evaluating the impact of different a priori knowledge on the crustal density profiles. Moreover, we applied both the original GEMMA algorithm [18] and the revised one (presented in the previous sections) to test their consistency. Thanks to closed-loop also the impact of forward linerization was tested. In the following subsection the "true" model and the possible scenarios will be described.

6.1. The "True" Model

The second radial derivative to be inverted was computed on a global $1^\circ \times 1^\circ$ grid at a constant altitude of 250 km, i.e., at the mean GOCE altitude, performing the forward modelling of the following layers: ice sheets, oceans, sediments, crystalline crust and uppermost mantle. The surfaces defining the interfaces between these layers are sampled on a $1^\circ \times 1^\circ$ spherical grid. The forward model was performed by numerical integration of dense point masses, generating a 3D simulated Earth model with point masses on a regular $0.1^\circ \times 0.1^\circ \times 100$ m lattice. Note that, according to the simulated gravity signal, all the inverse solutions computed in the following will have a $1^\circ \times 1^\circ$ resolution.

The boundaries of ice sheets, bathymetry and topography (the latter used as the top of sediments or of the crystalline crust, depending on the considered region) are taken from ETOPO1 [33], while the densities of ice and water are fixed to $\rho_{\mathrm{ICE}} = 980$ kg/m^3 and

$\rho_{OCE} = 1020\ \mathrm{kg/m^3}$, respectively. Sediments boundaries and densities are taken from the CRUST 1.0 model [6].

The crust density $\rho_C(\vartheta, \lambda, r)$ is defined by dividing it into 139 geological provinces according to the USGS map [34], adding the mid-oceanic ridges taken from the model by Coffin et al. [35]. Each province is classified as one of the main eight crustal types, i.e., shield, platform, orogenetic crust, basin, large igneous province, oceanic crust and mid-oceanic ridge (see Figure 4). As for the vertical density profile $\rho_{C,i}(r)$ of the i-th geological province (see Equation (25)), it is chosen depending on the type of the province itself (see [32,36,37]), according to the modellization introduced in the GEMMA model [18]. The chosen profiles are shown in Figure 5.

The upper mantle density $\rho_M(\vartheta, \lambda)$ is taken from the GyPSuM model [38] and does not contain any vertical variation. The upper mantle layer is modelled down to 100 km depth, assuming that there are no lateral density variations in the middle and lower mantle and inside the core. In fact, even if modelled, these lateral density variations would have an impact to the observed signal that is orders of magnitude smaller than the one due to crustal masses, and, in any case, they would be mainly concentrated at very long wavelengths [39].

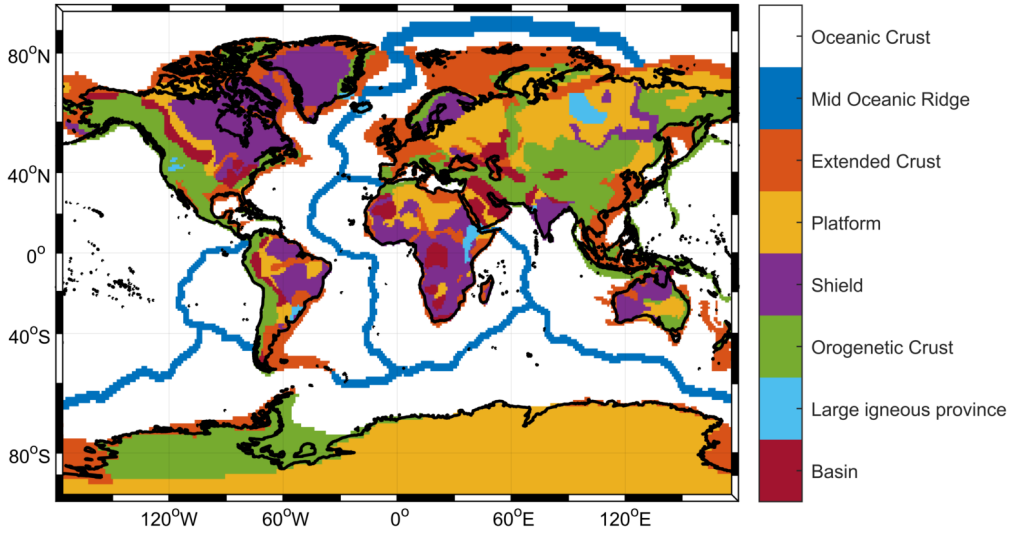

Figure 4. Map of geological provinces used to simulate the observed gravity signal.

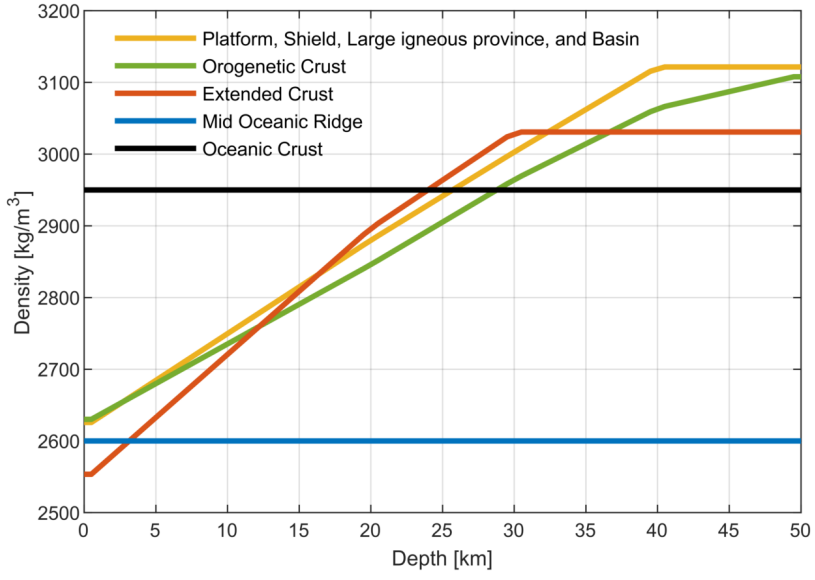

Figure 5. Density profiles of each type of crust used to simulate the observed gravity signal.

6.2. Tested Scenarios

To perform our closed-loop tests we are going to define three scenarios, where a decreasing level of knowledge (with respect to the true model) on the a priori density profiles is supposed. In particular, the three considered scenarios are:

s1. the a priori density profiles of all geological provinces are assumed to be the same as the "true" ones;
s2. the a priori density profiles of all geological provinces are assumed to be the same as the "true" ones apart from a scale factor (a different value of the scale factor for each geological type was applied, see Table 1);
s3. the a priori density profiles of all geological provinces are assumed to be the same as the "true" ones apart from a scale factor and a bias (a different couple of scale factor and bias for each geological type was applied, see Table 1).

Table 1. "True" scale factors (h) and biases (k) chosen in the three different scenarios for all the provinces belonging to the same crustal type.

Crustal Type	h			k [kg/m^3]		
	s1	**s2**	**s3**	**s1**	**s2**	**s3**
Oceanic	1.0000	0.9987	1.0020	0.00	0.00	0.00
Mid oceanic ridge	1.0000	1.0013	0.9977	0.00	0.00	0.00
Extended crust	1.0000	0.9910	0.9800	0.00	0.00	31.07
Platform	1.0000	1.0068	1.0150	0.00	0.00	−15.39
Shield	1.0000	1.0045	1.0100	0.00	0.00	−6.26
Orogenetic crust	1.0000	1.0090	1.0200	0.00	0.00	−66.60
Igneous provinces	1.0000	0.9955	0.9900	0.00	0.00	40.26
Basin	1.0000	0.9932	0.9850	0.00	0.00	49.39

As for the seismic information, it provides the geometrical shape of Moho surface. The observations of the Moho depth are simulated by corrupting its "true" value with a white random noise. The standard deviation of this noise is defined according to the reliability of the CRUST 2.0 model, which spatial distribution is shown in Figure 6 (for further details see [19]).

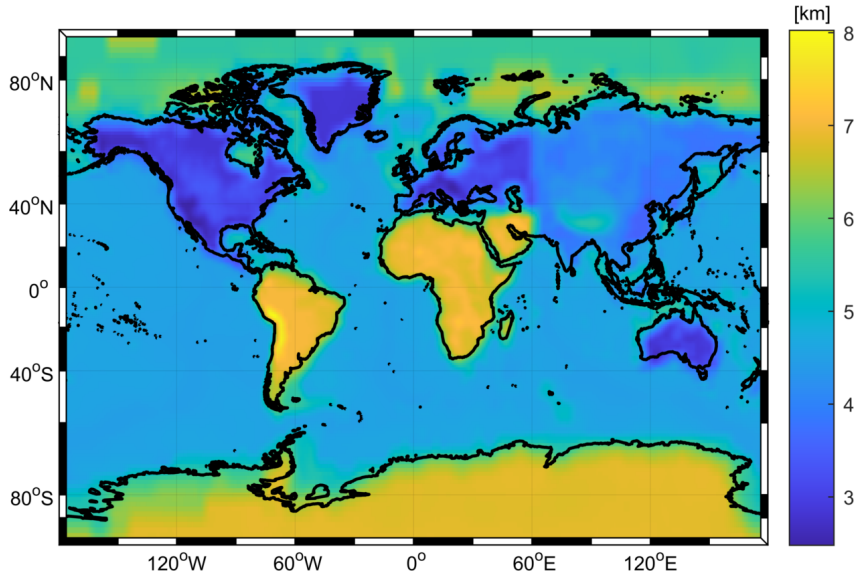

Figure 6. Standard deviation of the error of the input a priori seismic observations according to the CRUST2.0 model.

Finally, the gravity observations are simulated by forward modelling from the "true" geometries and densities by adding a randomly sampled noise, according to the degree

variances provided by the GO_CONS_GCF_2_TIM_R6 model [40,41]. The mentioned degree varainces and the sampled noise realization are shown in Figure 7.

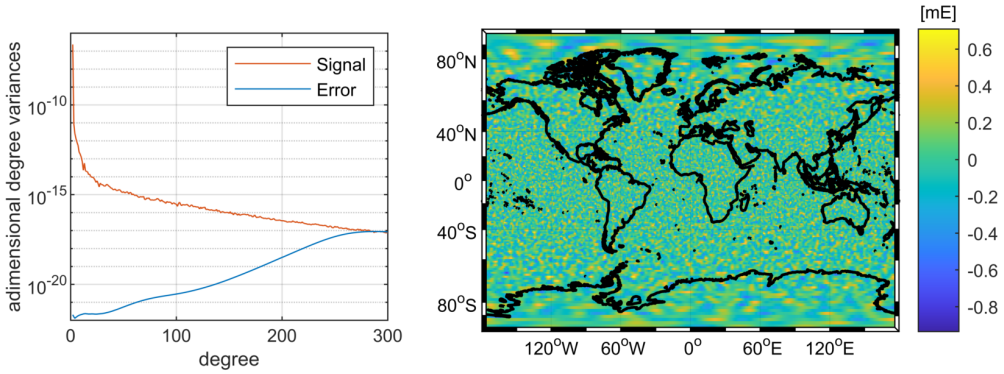

(**a**) Noise degree variances (**b**) Noise spatial distribution

Figure 7. Noise of the simulated gravity signal in terms of second radial derivative.

7. Algorithm Convergence

The convergence of the solution was tested by initializing the iterative procedure with different shapes of the Moho undulation. The s2 scenario was used for this purpose, even though completely similar results can be found by s1 or s3. In particular, two cases were mainly tested:

s2a. the Moho undulation at the beginning of the first iteration is equal to 0 everywhere, i.e., $\delta R_0(\vartheta, \lambda) = 0 \ \forall \ (\vartheta, \lambda)$;

s2b. the Moho undulation at the beginning of the first iteration is equal to the "true" one, i.e., $\delta R_0(\vartheta, \lambda) = \delta R_{\text{true}}(\vartheta, \lambda)$.

In both the cases, the convergence threshold was chosen as twice the vertical discretization step in the forward algorithm, in this case 2×100 m $= 200$ m. The iterative procedure is stopped when the maximum of the absolute difference between the Moho depth estimated at the current iteration and the previous one is below the chosen convergence threshold. Both the tests satisfied this convergence criterion in about 10 iterations. Nevertheless, most of the points of the Moho surface reach stability after three or four iterations, as shown by Figures 8 and 9, where the evolution of the iterative procedure is represented for s2a case.

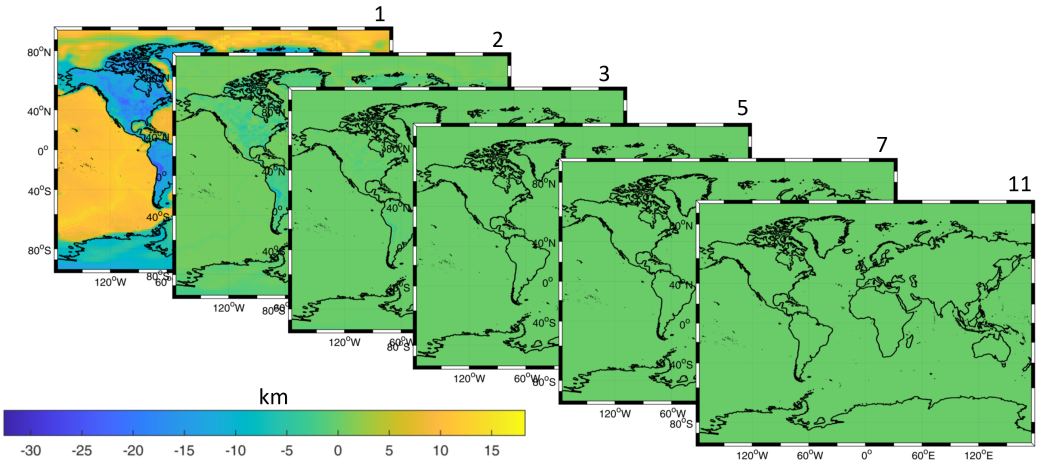

Figure 8. Maps of the Moho depth differences between an iteration and the previous one, showing the evolution of the algorithm for the s2a case ($\delta D_0(\vartheta, \lambda) = 0 \ \forall \ (\vartheta, \lambda)$).

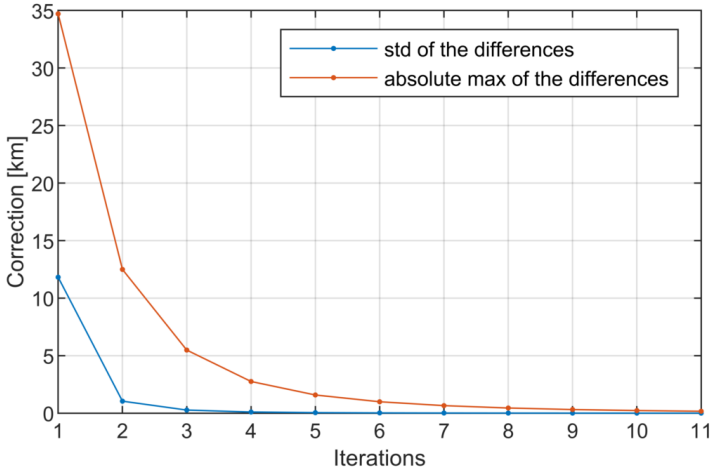

Figure 9. Statistics (standard deviation in blue and maximum of the absolute value in red) of the Moho depth differences between an iteration and the previous one, showing the convergence of the algorithm for the s2a case ($\delta R_0(\vartheta, \lambda) = 0 \ \forall \ (\vartheta, \lambda)$).

The behaviour of the iterative procedure is quite similar for the s2b case, showing that the solutions obtained by changing the starting point are basically equivalent. Their differences are always smaller than twice the modulus of the convergence threshold, i.e., the maximum admitted difference given the chosen convergence criterion, as shown in in Figure 10. Here the differences between the two solutions (s2a vs. s2b) in terms of estimated Moho depth are depicted.

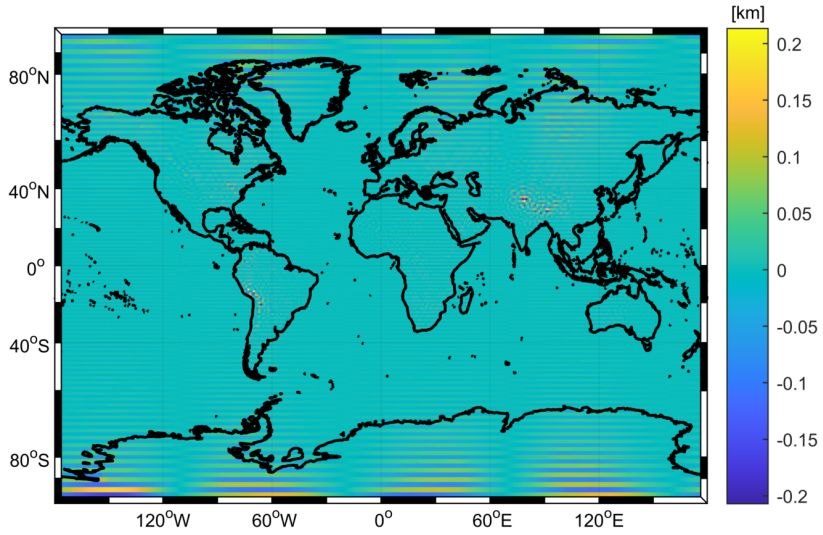

Figure 10. Map of the differences between the estimated Moho obtained starting from two different initial points (zero undulation vs. true Moho, namely s2a and s2b, respectively).

As for the estimated values of the h_i and k_i parameters for each geological province the estimations obtained changing the starting point are completely consistent too. In fact, they show a relative difference smaller than 0.003% for all the h_i parameters and an absolute difference smaller than 0.01 kg/m^3 for all the k_i parameters, as shown in Figure 11.

These tests show that the algorithm is converging to the same solution if the algorithm is initialized to a reasonable starting point, and that the flat Moho is included in the set of allowed starting point. This is fully compatible with the assumption performed by linearizing the Newton integral in Equation (5).

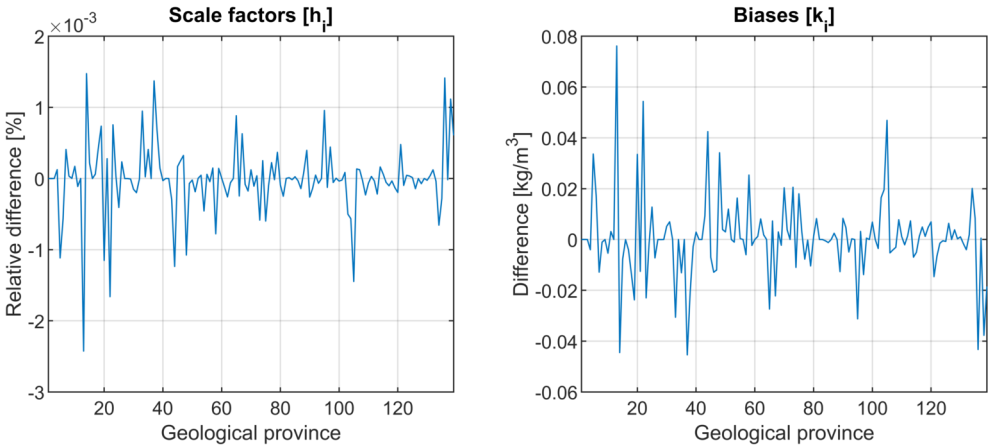

Figure 11. On the **left panel**, relative differences between the parameters h_i estimated for each geological province changing the starting point of the iterative solution (zero undulation vs. true Moho, namely s2a and s2b, respectively). On the **right panel**, absolute differences between the parameters k_i estimated for each geological province changing the starting point of the iterative solution (zero undulation vs. true Moho, namely s2a and s2b, respectively). In both the graphs the geological provinces are represented on the abscissa and the differences on the ordinate.

8. Impact of the Forward Approximations

To check the impact of the approximations introduced in the inversion procedure by the linearization of the forward operator (see Equation (5)), two solutions were computed considering the s2 scenario. The two tests differ in the kind of forward operators used in the data reduction of Equation (21). The former solution (s2c) is obtained by applying Equation (21) as is, i.e., it is applied as explained in the revised algorithm. The latter solution (s2d) is obtained by introducing the $\mathcal{F}_{rr}(\cdot)$ operator instead of the $\widetilde{\mathcal{F}}_{rr}(\cdot)$ linearized one $\widetilde{\mathcal{F}}_{rr}(\cdot)$ into Equation (21), as it was performed in the original GEMMA algorithm, but without implementing the last step for the reference Moho improvement (Section 2.4 of [18]). The results of the s2c and s2d solutions show that the standard deviation of the gravity gradient residuals is 3.2 mE in the first case, while it grows up to 36.2 mE in the second one. To give an interpretation to this discrepancy, it is interesting to compare the inversion residuals with the forward linearization approximation. This approximation is represented in Figure 12 and can be seen as the difference between the forward of the density contrast inside the "true" Moho undulation computed by $\mathcal{F}_{rr}(\cdot)$ and the same quantity computed by $\widetilde{\mathcal{F}}_{rr}(\cdot)$. The standard deviation of this approximation effect is about 36 mE.

The comparison between the inversion residuals and the forward approximation is performed in terms of linear correlation coefficients as shown in Figure 13. Here, it is clearly visible that the s2d solution (without considering linearized forward in Equation (21)) is highly correlated with the forward approximation. Therefore, the proper combination of the two kinds of forward operators ($\mathcal{F}_{rr}(\cdot)$ and $\widetilde{\mathcal{F}}_{rr}(\cdot)$ in Equation (21) allows to overcome this drawback.

Since the solution with the "full" original GEMMA algorithm, also including the reference Moho improvement step, is substantially equivalent to the one of the revised algorithm, as we will see in the next section, it is clear that the main goal of the reference Moho improvement step was to filter out the linearization error shown in Figure 12. On the other hand, it is also clear that this step is not anymore required in the revised algorithm, also implying a gain in terms of computation time.

Repeating the comparisons performed in this section for the s1 or s3 scenarios, the obtained results would show an analogous behaviour.

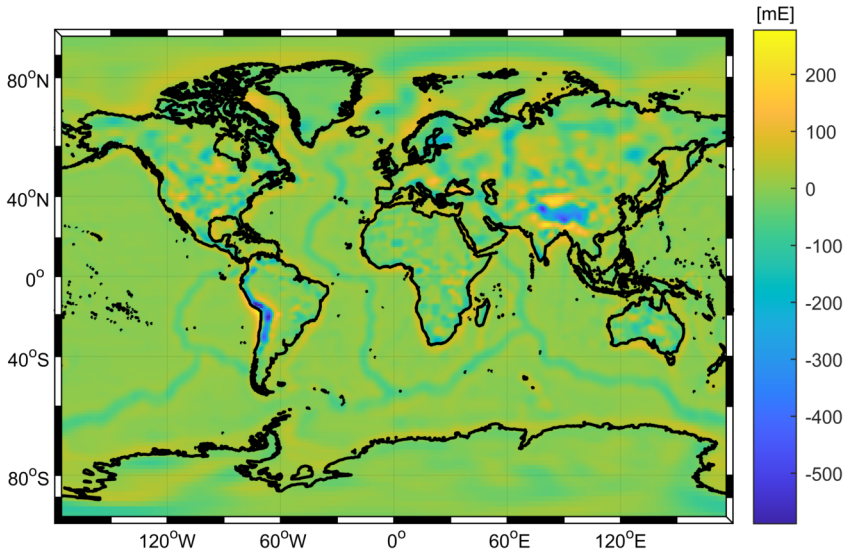

Figure 12. Differences between the forward of the Moho undulation computed applying the $\mathcal{F}_{rr}(\cdot)$ or $\widetilde{\mathcal{F}}_{rr}(\cdot)$ operator.

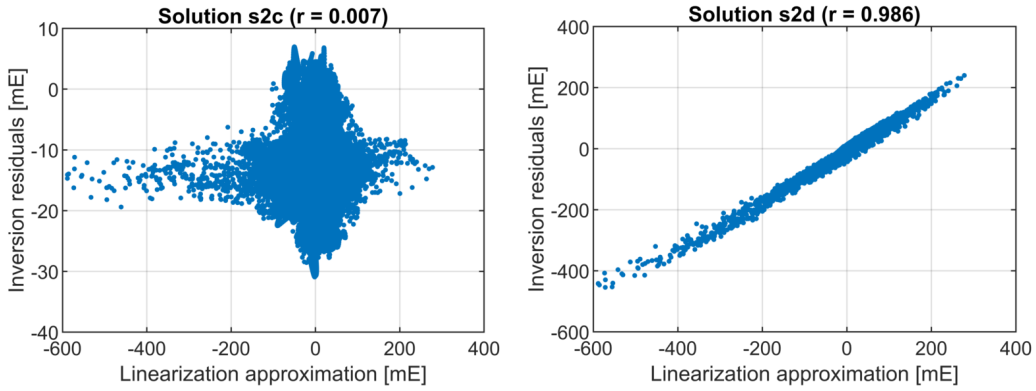

Figure 13. Linear correlation between the residuals of the inversion and the linearization approximation in: solution using Equation (21) as is (s2c), and solution with the $\mathcal{F}_{rr}(\cdot)$ operator in place of the $\widetilde{\mathcal{F}}_{rr}(\cdot)$ one into Equation (21) (s2d).

9. Comparison of the Original and Revised Algorithms

In this section the results of the closed-loop gravity inversion by using the original (denoted with O, see [18,19]) and the revised (denoted with R, see Sections 2–5) algorithms with the input of the three scenarios presented in Section 6.2 are compared. These comparisons aim at verifying the consistency between the two algorithms, as well as their capability of retrieving the "true" shape of the model. In particular, the differences between the estimates of the Moho surface coming from the two algorithms, i.e., $\widehat{D}^{\mathrm{R}} - \widehat{D}^{\mathrm{O}}$, and the differences between the forwarded gravitational signal coming from the solutions of the two algorithms, i.e., $\widehat{T}^{\mathrm{R}}_{rr} - \widehat{T}^{\mathrm{O}}_{rr}$, are first evaluated and then used to set up some statistical tests at both global and local level.

In particular, we performed the following tests assuming a significance level $\alpha = 5\%$:

1. a global test on the differences between the Moho estimates, i.e.,

$$\frac{\mathcal{M}\left[\widehat{D}^{\mathrm{R}} - \widehat{D}^{\mathrm{O}}\right]}{\mathcal{S}\left[\widehat{D}^{\mathrm{R}} - \widehat{D}^{\mathrm{O}}\right]} \sim Z \tag{32}$$

where the operators $\mathcal{M}[\cdot]$ and $\bar{\mathcal{S}}[\cdot]$ are the mean and standard deviation computed over all Moho grid nodes, respectively;

2. a global test between the differences of the forwarded gravitational signal of the estimated models, i.e.,

$$\frac{\mathcal{M}\left[\widehat{T}_{rr}^{\mathrm{R}} - \widehat{T}_{rr}^{\mathrm{O}}\right]}{\bar{\mathcal{S}}\left[\widehat{T}_{rr}^{\mathrm{R}} - \widehat{T}_{rr}^{\mathrm{O}}\right]} \sim Z \tag{33}$$

3. local tests on the Moho differences, by comparing the discrepancy of the two solutions on subsets of grid nodes defined on the basis of the "true" Moho depth. In particular, the subsets are obtained by splitting the "true" Moho depth in 1 km classes. The statistic of the test becomes

$$\frac{\mathcal{M}\left[\widehat{D}_{j}^{\mathrm{R}} - \widehat{D}_{j}^{\mathrm{O}}\right]}{\bar{\mathcal{S}}\left[\widehat{D}_{j}^{\mathrm{R}} - \widehat{D}_{j}^{\mathrm{O}}\right]} \sim Z \tag{34}$$

where the index j identifies the class corresponding to a given reference Moho depth.

4. local tests on the Moho differences, by comparing the discrepancy of the two solutions on subsets of grid nodes defined as the geological provinces, i.e.,

$$\frac{\mathcal{M}\left[\widehat{D}_{i}^{\mathrm{R}} - \widehat{D}_{i}^{\mathrm{O}}\right]}{\bar{\mathcal{S}}\left[\widehat{D}_{i}^{\mathrm{R}} - \widehat{D}_{i}^{\mathrm{O}}\right]} \sim Z \tag{35}$$

where the index i identifies the given geological province.

The statistics and the outcome of the global tests (1 and 2) are summarized in Tables 2 and 3, while Figures 14 and 15 show the results of the tests 3 and 4, respectively.

Table 2. Statistics on the differences of the Moho estimated by the two algorithms, $\widehat{D}^{\mathrm{R}} - \widehat{D}^{\mathrm{O}}$, for the three tested scenarios.

Scenario	Mean [km]	Std [km]	Max [km]	Min [km]	Test 1
s1	0.22	0.66	9.95	−13.25	0.33 < 1.96
s2	0.55	1.01	10.31	−12.91	0.55 < 1.96
s3	0.48	0.99	10.02	−12.78	0.49 < 1.96

Table 3. Statistics on the differences of the forwarded gravitational signal from the solutions estimated by the two algorithms, $\widehat{T}_{rr}^{\mathrm{R}} - \widehat{T}_{rr}^{\mathrm{O}}$, for the three tested scenarios.

Scenario	Mean [mE]	Std [mE]	Max [mE]	Min [mE]	Test 2
s1	−6.47	3.58	15.71	−72.01	1.80 < 1.96
s2	0.59	3.67	22.91	−63.89	0.16 < 1.96
s3	−1.32	3.60	20.19	−67.67	0.37 < 1.96

From the outcome of these tests it is quite clear that the two algorithms perform in a very similar way, with no significant differences from a statistical point of view at a global level (see the results of tests 1 and 2) and with small differences at local level. The latter could depend on slightly different regularization procedures when the vertical density profiles of the geological provinces have to be adjusted by Least Squares (see Section 4). Note that the regularization procedures are different because the set of parameters to be estimated is different, due to the introduction of biases k_i in the revised version. Therefore, in the following, we will consider the revised algorithm only, comparing it with the truth to assess its performances. Tables 4 and 5 show the differences between the solution and the truth for the different scenarios in terms of estimated Moho depth and gravity gradient residuals.

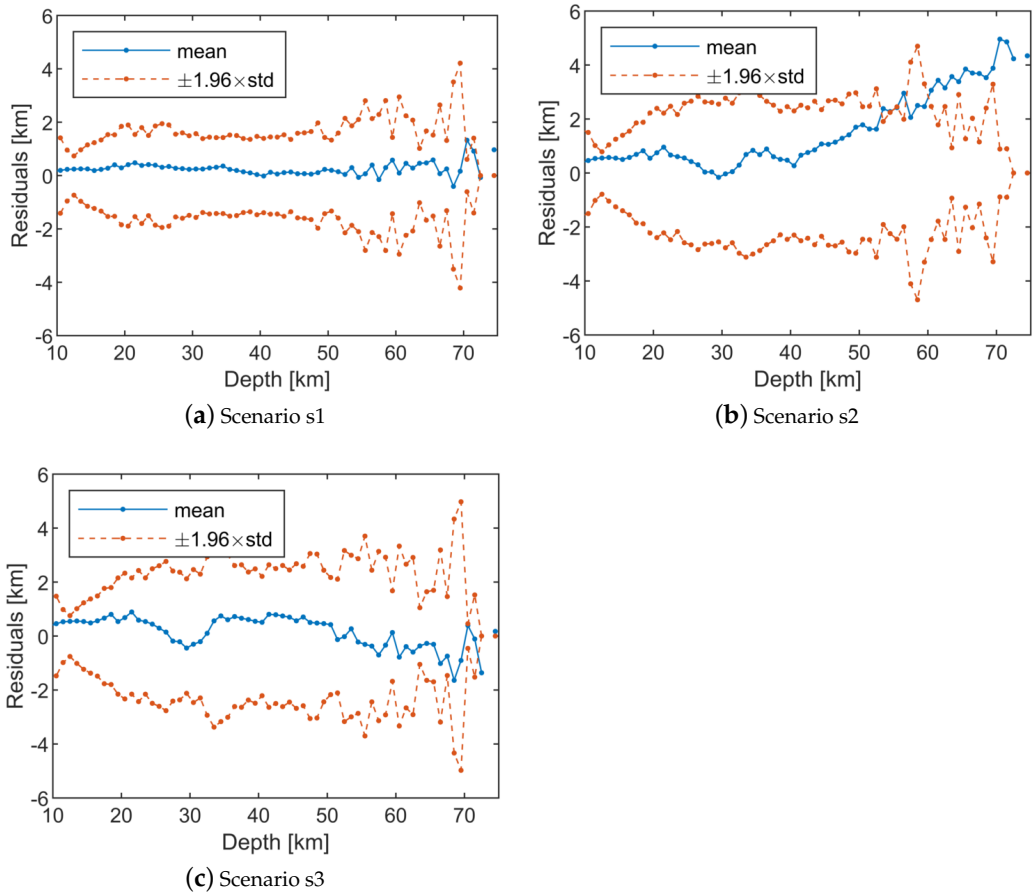

(**a**) Scenario s1 (**b**) Scenario s2

(**c**) Scenario s3

Figure 14. Results of test 3. On the abscissa the reference Moho depth, on the ordinate the statistics of the Moho differences for the corresponding subset of grid nodes. Blue line represents the mean of the differences, and the red ones represent the confidence interval depending on the standard deviation and the level of significance.

Table 4. Statistics on the differences between the estimated and "true" Moho, $\widehat{D}^{\mathrm{R}} - D^{\mathrm{true}}$, for the three tested scenarios. The test 1 is implemented as in Equation (32) by replacing $\widehat{D}^{\mathrm{O}}$ with D^{true}.

Scenario	Mean [km]	Std [km]	Max [km]	Min [km]	Test 1
s1	0.01	0.76	12.10	−8.18	0.01 < 1.96
s2	0.01	1.26	12.03	−12.14	0.01 < 1.96
s3	0.06	1.23	12.18	−10.24	0.05 < 1.96

Table 5. Statistic on the differences between the forwarded gravitational signal from revised algorithm solution and from the "true" model, $\widehat{T}_{rr}^{\mathrm{R}} - T_{rr}^{\mathrm{true}}$, for the three tested scenarios. The test 2 is implemented as in Equation (33) by replacing $\widehat{T}_{rr}^{\mathrm{O}}$ with T_{rr}^{true}.

Scenario	Mean [mE]	Std [mE]	Max [mE]	Min [mE]	Test 2
s1	−6.25	3.20	13.66	−24.54	1.95 < 1.96
s2	0.72	3.22	20.55	−17.70	0.22 < 1.96
s3	−1.15	3.21	18.28	−20.03	0.36 < 1.96

The comparison with respect to the "true" model in terms of estimated Moho depth (see Table 4) clearly show the ability of the algorithm in retrieving the original shape of the Moho with an accuracy of the order of 1 km, although the range of the differences is one order of magnitude larger. However, the highest values in the differences are related to the

high frequencies patterns of the true Moho surface, e.g., close to the continental-oceanic boundaries or the mid-oceanic ridges, that are over-smoothed in the Moho estimate. This effect is mainly related to the isotropic assumption in the definition of the Moho spectrum to be used in the Wiener filtering procedure (see Equation (17)). This unique global Moho spectrum cannot follow the local high frequencies of the Moho surface.

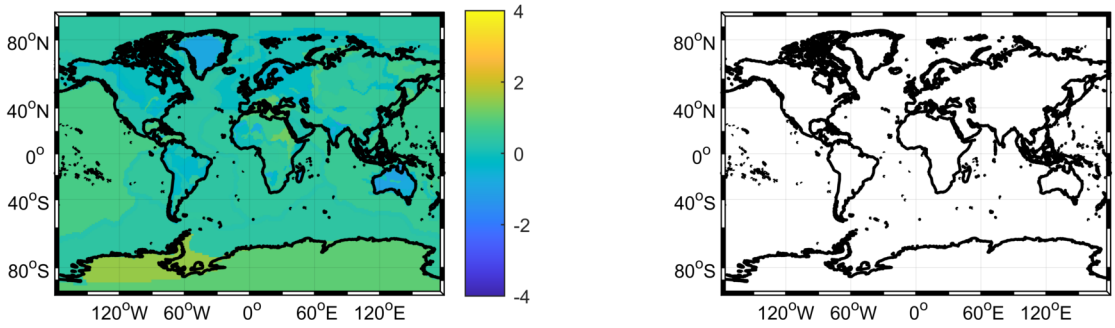

(**a**) Scenario s1

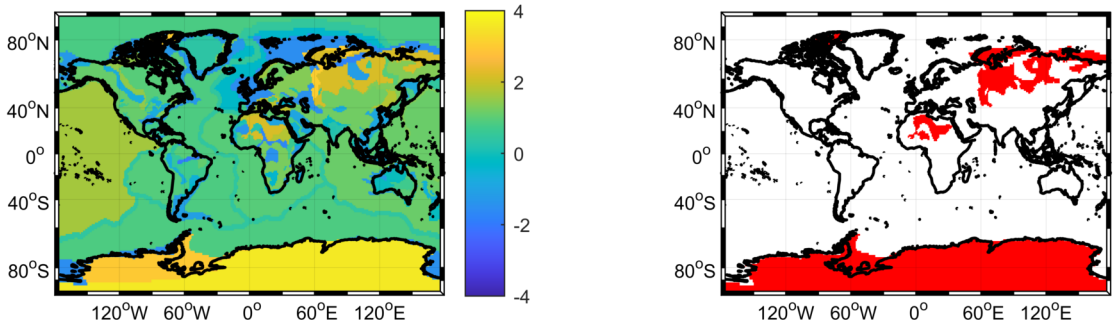

(**b**) Scenario s2

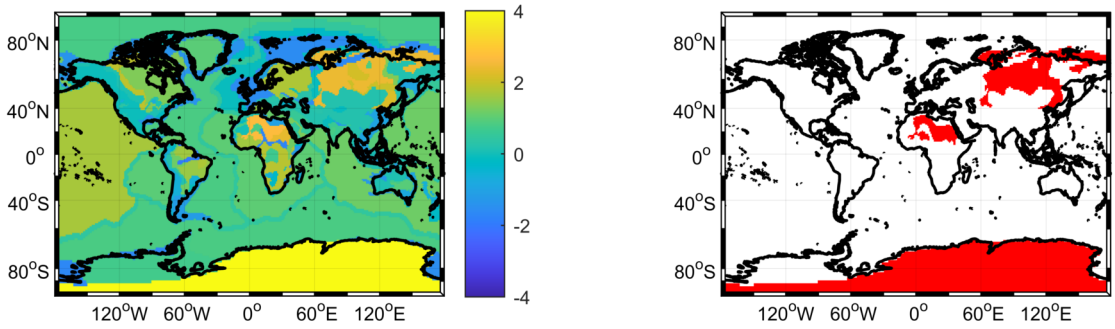

(**c**) Scenario s3

Figure 15. Results of test 4. For each scenario, the empirical value of the statistics on the left, and in red the geological provinces for which the consistency hypothesis is rejected on the right.

As for the gravity gradient residuals, the estimated models lead to fit the signal with a standard deviation of about 3 mE, which is comparable with the standard deviation of the observation noise, showing the capability of the presented algorithm of correctly explaining the data.

10. Conclusions

In this work we revised the gravity inversion algorithm used to compute the GEMMA Moho model in 2015 [18]. The aim was to improve this algorithm from the formalization and numerical points of view. The former allows an easier way to introduce the algorithm parameters (e.g., the observation noise covariance into the Wiener filter) and a more formal

management of the approximation related to the linearization of the forward operator. The latter turns into a reduction of the computational time, giving the possibility of performing extensive tests by means of closed-loop scenarios.

By exploiting these closed-loop tests, it become possible to analyse the algorithm convergence, to verify the algorithm capability of retrieving a known Moho depth, and to study the the impact of using a linearized relation in the inversion procedure (see Equation (5)). The results show that:

- the iterative inversion algorithm converges to a unique solution (disregarding differences smaller than the iteration stop criterion) when changing the starting point, e.g., choosing an a priori Moho undulation ranging from zero to the "true" value;
- the Moho depth is retrieved with an accuracy of the order of 1 km (in terms of standard deviation), consistently with the solution coming from the original GEMMA algorithm;
- the effect of the linearization is analytically controlled through a suitable data reduction, without the need of a further step in the inversion procedure for the reference Moho refinement, as it happened in the original GEMMA algorithm.

This work will make possible to improve the GEMMA model in the future, by integrating newly available datasets, from both the gravity and geophysical sides. As for the former, improved GOCE global gravity models were released in the meanwhile, arriving at the sixth release, while only the second release was used in the GEMMA solution of 2015. As for the latter, also new geophysical models were released in the meanwhile, e.g., high resolution maps of sediments, the CRUST1.0 model, etc. Therefore, the target is to ingest this enhanced knowledge to release a new gravity-based crustal model, and this work lays the foundations for it from the algorithmic point of view.

Author Contributions: Conceptualization, all authors; methodology, L.R. and M.R.; software: L.R., B.L. and M.R; validation, L.R. and B.L.; formal analysis, L.R. and M.R.; investigation, all authors; data curation, L.R., B.L., I.F., D.S. and M.R.; writing—original draft preparation, L.R.; writing—review and editing, all authors; visualization, L.R.; supervision, M.R. and M.v.d.M. All authors have read and agreed to the published version of the manuscript.

Funding: This research was funded by Dutch Research Council, Grant No. ALWGO.2017.030.

Data Availability Statement: The data presented in this study are available on request from the corresponding author. The data are not publicly available due to storage limitation.

Conflicts of Interest: The authors declare no conflict of interest.

Abbreviations

The following abbreviations are used in this manuscript:

GEMMA	GOCE Exploitation for Moho Modelling and Applications
GOCE	Gravity Field and Steady-State Ocean Circulation Explorer
std	Standard deviation
PREM	Preliminary reference Earth model

References

1. Mohorovičić, A. Earthquake of 8 October 1909. *Geofizika* **1992**, *9*, 3–55. English translation from: Potres od 8. X. 1909, Godišnje izvješće zagrebačkig meteorološkog observatorija za godiun 1909, godina IX, dio IV, polovina 1, 1–56 (1910).
2. Gutenberg, B. Channel waves in the Earth's crust. *Geophysics* **1955**, *20*, 283–294. [CrossRef]
3. Soller, D.R.; Ray, R.D.; Brown, R.D. A new global crustal thickness map. *Tectonics* **1982**, *1*, 125–149. [CrossRef]
4. Mooney, W.D.; Laske, G.; Masters, T.G. CRUST 5.1: A global crustal model at 5 × 5. *J. Geophys. Res. Solid Earth* **1998**, *103*, 727–747. [CrossRef]
5. Bassin, C.; Laske, G.; Masters, G. The current limits of resolution for surface wave tomography in North America. *Eos Trans. Am. Geophys. Union* **2000**, *81*, F897.
6. Laske, G.; Masters, G.; Ma, Z.; Pasyanos, M. Update on CRUST1. 0—A 1-degree global model of Earth's crust. In Proceedings of the Geophysical Research Abstracts. EGU General Assembly, Vienna, Austria, 7-12 April 2013; Volume 15, p. 2658.

7. Szwillus, W.; Afonso, J.C.; Ebbing, J.; Mooney, W.D. Global Crustal Thickness and Velocity Structure From Geostatistical Analysis of Seismic Data. *J. Geophys. Res. Solid Earth* **2019**, *124*, 1626–1652. [CrossRef]
8. Heiskanen, W. The geophysical applications of gravity anomalies. *Eos Trans. Am. Geophys. Union* **1953**, *34*, 11–15. [CrossRef]
9. Talwani, M.; Worzel, J.L.; Landisman, M. Rapid gravity computations for two-dimensional bodies with application to the Mendocino submarine fracture zone. *J. Geophys. Res.* **1959**, *64*, 49–59. [CrossRef]
10. Talwani, M.; Ewing, M. Rapid computation of gravitational attraction of three-dimensional bodies of arbitrary shape. *Geophysics* **1960**, *25*, 203–225. [CrossRef]
11. Oldenburg, D.W. The inversion and interpretation of gravity anomalies. *Geophysics* **1974**, *39*, 526–536. [CrossRef]
12. Parker, R. The rapid calculation of potential anomalies. *Geophys. J. Int.* **1973**, *31*, 447–455. [CrossRef]
13. Braitenberg, C.; Pettenati, F.; Zadro, M. Spectral and classical methods in the evaluation of Moho undulations from gravity data: The NE Italian Alps and isostasy. *J. Geodyn.* **1997**, *23*, 5–22. [CrossRef]
14. Barzaghi, A.; Gandino, A.; Sansò, F.; Zenucchini, C. The collocation approach to the inversion of gravity data. *Geophys. Prospect.* **1992**, *40*, 429–451. [CrossRef]
15. Chen, W.; Tenzer, R. Moho modeling using FFT technique. *Pure Appl. Geophys.* **2017**, *174*, 1743–1757. [CrossRef]
16. Sjöberg, L.E.; Bagherbandi, M. A method of estimating the Moho density contrast with a tentative application of EGM08 and CRUST2.0. *Acta Geophys.* **2011**, *59*, 502–525. [CrossRef]
17. Sjöberg, L.E.; Bagherbandi, M. *Gravity Inversion and Integration*; Springer: Cham, Switzerland 2017.
18. Reguzzoni, M.; Sampietro, D. GEMMA: An Earth crustal model based on GOCE satellite data. *Int. J. Appl. Earth Obs. Geoinf.* **2015**, *35*, 31–43. [CrossRef]
19. Reguzzoni, M.; Sampietro, D.; Sansò, F. Global Moho from the combination of the CRUST2.0 model and GOCE data. *Geophys. J. Int.* **2013**, *195*, 222–237. [CrossRef]
20. Tenzer, R.; Hamayun; Novák, P.; Gladkikh, V.; Vajda, P. Global crust-mantle density contrast estimated from EGM2008, DTM2008, CRUST2. 0, and ICE-5G. *Pure Appl. Geophys.* **2012**, *169*, 1663–1678. [CrossRef]
21. MacMillan, W.D. *The Theory of the Potential*; Dover Publications: New York, NY, USA, 1958.
22. Strang van Hees, G.L. Some elementary relations between mass distributions inside the Earth and the geoid and gravity field. *J. Geodyn.* **2000**, *29*, 111–123. [CrossRef]
23. Sjöberg, L.E. Solving Vening Meinesz-Moritz inverse problem in isostasy. *Geophys. J. Int.* **2009**, *179*, 1527–1536. [CrossRef]
24. Bagherbandi, M.; Eshagh, M. Recovery of Moho's undulations based on the Vening Meinesz–Moritz theory from satellite gravity gradiometry data: A simulation study. *Adv. Space Res.* **2012**, *49*, 1097–1111. [CrossRef]
25. Bagherbandi, M.; Tenzer, R.; Sjöberg, L.E.; Novák, P. Improved global crustal thickness modeling based on the VMM isostatic model and non-isostatic gravity correction. *J. Geodyn.* **2013**, *66*, 25–37. [CrossRef]
26. Reguzzoni, M.; Sampietro, D. An inverse gravimetric problem with GOCE data. In *Proceedings of the Gravity, Geoid and Earth Observation*; Mertikas, S.P., Ed.; International Association of Geodesy Symposia; Springer: Berlin/Heidelberg, Germany, 2010; Volume 135, pp. 451–456. [CrossRef]
27. Heiskanen, W.A.; Moritz, H. *Physical Geodesy*; W. H. Freeman and Company: San Francisco, CA, USA 1967.
28. Papoulis, A. *Signal Analysis*; McGraw-Hill: New York, NY, USA, 1977.
29. Drinkwater, M.R.; Floberghagen, R.; Haagmans, R.; Muzi, D.; Popescu, A., GOCE: ESA's First Earth Explorer Core Mission. In *Earth Gravity Field from Space—From Sensors to Earth Sciences: Proceedings of an ISSI Workshop 11–15 March 2002, Bern, Switzerland*; Beutler, G., Drinkwater, M.R., Rummel, R., Von Steiger, R., Eds.; Springer: Dordrecht, The Netherlands, 2003; pp. 419–432. [CrossRef]
30. Rummel, R.; Yi, W.; Stummer, C. GOCE gravitational gradiometry. *J. Geod.* **2011**, *85*, 777–790. [CrossRef]
31. Dziewonski, A.M.; Anderson, D.L. Preliminary reference Earth model. *Phys. Earth Planet. Inter.* **1981**, *25*, 297–356. [CrossRef]
32. Christensen, N.I.; Mooney, W.D. Seismic velocity structure and composition of the continental crust: A global view. *J. Geophys. Res. Solid Earth* **1995**, *100*, 9761–9788. [CrossRef]
33. Amante, C.; Eakins, B.W. ETOPO1 1 arc-minute global relief model: Procedures, data sources and analysis. In *NOAA Technical Memorandum NESDIS NGDC-24*; National Centers for Environmental Information: Silver Spring, MD, USA, 2009. [CrossRef]
34. Exxon. *Tectonic Map of the World, 18 sheets, scale 1:10,000,000*; 594 Technical Report; Exxon: Houston , TX, USA, 1995
35. Coffin, M.; Gahagan, L.; Lawver, L. *Present-day plate boundary digital data compilation*; UTIG Technical Report No. 174; University of Texas: Austin, TX, USA, 1995.
36. Carlson, R.; Raskin, G. Density of the ocean crust. *Nature* **1984**, *311*, 555–558. [CrossRef]
37. Lin, J.; Morgan, J.P. The spreading rate dependence of three-dimensional mid-ocean ridge gravity structure. *Geophys. Res. Lett.* **1992**, *19*, 13–16. [CrossRef]
38. Simmons, N.A.; Forte, A.M.; Boschi, L.; Grand, S.P. GyPSuM: A joint tomographic model of mantle density and seismic wave speeds. *J. Geophys. Res. Solid Earth* **2010**, *115*, B12310. [CrossRef]
39. Hager, B.H.; Clayton, R.W.; Richards, M.A.; Comer, R.P.; Dziewonski, A.M. Lower mantle heterogeneity, dynamic topography and the geoid. *Nature* **1985**, *313*, 541–545. [CrossRef]

40. Brockmann, J.M.; Schubert, T.; Schuh, W.D. An Improved Model of the Earth's Static Gravity Field Solely Derived from Reprocessed GOCE Data. *Surv. Geophys.* **2021**, *42*, 277–316. [CrossRef]
41. Brockmann, J.M.; Schubert, T.; Mayer-Gürr, T.; Schuh, W.D. The Earth's Gravity Field as Seen by the GOCE Satellite—An Improved Sixth Release Derived with the Time-Wise Approach (GO_CONS_GCF_2_TIM_R6); In *GFZ Data Services*; ICGEM: Toulouse, France, 2019. [CrossRef]